

# VIRIAL MASSES AND THE BARYON FRACTION IN GALAXIES<sup>1</sup>

H. HOEKSTRA,<sup>2,3,4</sup> B. C. HSIEH,<sup>5,6</sup> H. K. C. YEE,<sup>4</sup> H. LIN,<sup>7</sup> AND M. D. GLADDERS<sup>8</sup>

Received 2005 April 28; accepted 2005 July 30

## ABSTRACT

We have measured the weak-lensing signal as a function of rest-frame  $B$ -,  $V$ -, and  $R$ -band luminosity for a sample of “isolated” galaxies. These results are based on four-band photometry from the Red-Sequence Cluster Survey, enabling us to determine photometric redshifts for a large number of galaxies. We select a secure sample of lenses with photometric redshifts  $0.2 < z < 0.4$  and study the relation between the virial mass and baryonic contents. In addition, we discuss the implications of the derived photometric redshift distribution for published cosmic shear studies. The virial masses are derived from a fit to the observed lensing signal. For a galaxy with a fiducial luminosity of  $10^{10} h^{-2} L_{B,\odot}$ , we obtain a mass  $M_{\text{vir}} = 9.9^{+1.5}_{-1.3} \times 10^{11} M_{\odot}$ . The virial mass as a function of luminosity is consistent with a power law  $\propto L^{1.5}$ , with similar slopes for the three filters considered here. These findings are in excellent agreement with results from the Sloan Digital Sky Survey and semianalytic models of galaxy formation. We measure the fraction of mass in stars and the baryon fraction in galaxies by comparing the virial mass-to-light ratio to predicted stellar mass-to-light ratios. We find that star formation is inefficient in converting baryons into stars, with late-type galaxies converting  $\sim 33\%$  and early-type galaxies converting only  $\sim 14\%$  of baryons into stars. Our results imply that the progenitors of early-type galaxies must have low stellar mass fractions, suggestive of a high formation redshift.

*Subject headings:* cosmology: observations — dark matter — galaxies: halos — gravitational lensing

*Online material:* color figures

## 1. INTRODUCTION

Observations of rotation curves of spiral galaxies and measurements of the velocity dispersions of stars in early-type galaxies have provided important evidence for the existence of massive dark matter halos around galaxies (e.g., van Albada & Sancisi 1986). In addition, these studies have presented evidence of tight relations between the baryonic and dark matter components (e.g., Tully & Fisher 1977; Faber & Jackson 1976). Results based on strong lensing by galaxies support these findings (e.g., Keeton et al. 1998).

The origin of these scaling relations must be closely related to the process of galaxy formation, but the details are still not well understood, mainly because of the complex behavior of the baryons. Furthermore, on the small scales where baryons play such an important role, the accuracy of cosmological numerical simulations is limited. This complicates a direct comparison of models of galaxy formation to observational data. For such applications, it would be more convenient to have observational constraints on quantities that are robust and easily extracted from numerical simulations.

An obvious choice is the virial mass of the galaxy, but most techniques for measuring mass require visible tracers of the potential, confining the measurements to relatively small radii. Fortunately, recent developments in weak gravitational lensing have made it possible to probe the ensemble-averaged mass distribution around galaxies out to large projected distances. The tidal gravitational field of the dark matter halo introduces small coherent distortions in the images of distant background galaxies, which can be easily detected in current large imaging surveys. We note that one can only study ensemble-averaged properties, because the weak-lensing signal induced by an individual galaxy is too small to be detected.

Since the first detection of this so-called galaxy-galaxy lensing signal by Brainerd et al. (1996), the significance of the measurements has improved dramatically, thanks to new wide-field CCD cameras on a number of mostly 4 m class telescopes. This has allowed various groups to image large areas of the sky, yielding the large numbers of lenses and sources needed to measure the lensing signal. For instance, Hoekstra et al. (2004) used  $45.5 \text{ deg}^2$  of  $R_C$ -band imaging data from the Red-Sequence Cluster Survey (RCS), enabling them to measure, for the first time, the extent and flattening of galaxy dark matter halos, providing strong support for the cold dark matter (CDM) paradigm. However, the analysis presented in Hoekstra et al. (2004) was based on the  $R_C$ -band data alone and consequently lacked redshift information for the individual lenses.

An obvious improvement is to obtain redshift information for the lenses (and, if possible, the sources). This allows one to study the lensing signal as a function of lens properties, most notably the luminosity. Photometric redshifts were used by Hudson et al. (1998) to scale the lensing signal of galaxies in the Hubble Deep Field and by Wilson et al. (2001), who measured the lensing signal around early-type galaxies as a function of redshift. Smith et al. (2001) and Hoekstra et al. (2003) used spectroscopic redshifts, but the lens samples involved were rather small ( $\sim 1000$ ). The Sloan Digital Sky Survey (SDSS) combines both survey area

<sup>1</sup> Based on observations from the Canada-France-Hawaii Telescope, which is operated by the National Research Council of Canada, the Institut National des Sciences de l’Univers of the Centre National de la Recherche Scientifique of France, and the University of Hawaii.

<sup>2</sup> Department of Physics and Astronomy, University of Victoria, P.O. Box 3055, Victoria, BC V8P 5C2, Canada.

<sup>3</sup> Canadian Institute for Theoretical Astrophysics, University of Toronto, 60 St. George Street, Toronto, ON M5S 3H8, Canada.

<sup>4</sup> Department of Astronomy and Astrophysics, University of Toronto, 60 St. George Street, Toronto, ON M5S 3H8, Canada.

<sup>5</sup> Institute of Astronomy, National Central University, 300 Jhongda Road, Jhongli City, Taoyuan County 320, Taiwan.

<sup>6</sup> Institute of Astrophysics and Astronomy, Academia Sinica, P.O. Box 23-141, Taipei 106, Taiwan.

<sup>7</sup> Fermi National Accelerator Laboratory, P.O. Box 500, 500 Wilson Road, Batavia, IL 60510.

<sup>8</sup> Carnegie Observatories, 813 Santa Barbara Street, Pasadena, CA 91101.

and redshift information. Its usefulness for galaxy-galaxy lensing was demonstrated clearly by Fischer et al. (2000). More recently, McKay et al. (2001) used the available SDSS redshift information to study the galaxy-galaxy lensing signal as a function of galaxy properties (also see Guzik & Seljak 2002; Seljak 2002; Sheldon et al. 2004).

In this paper we use a subset of the RCS data for which photometric redshifts have been determined using  $B$ ,  $V$ ,  $R_C$ , and  $z'$  data taken using the Canada-France-Hawaii Telescope (CFHT; see Hsieh et al. 2005 for details). The area covered by these multiwavelength data is approximately  $33.6 \text{ deg}^2$ , resulting in a catalog of  $1.2 \times 10^6$  galaxies for which a redshift could be determined, making it one of the largest data sets of its kind. This unique data set allows us to measure the virial masses of galaxies as a function of their luminosity.

This paper is structured as follows. In § 2 we briefly discuss the data, including the photometric redshift catalog and its accuracy. The results of some basic tests of the photometric redshifts are presented in § 3. In § 4 we discuss the dark matter profile inferred from numerical simulations. The measurement of the virial mass as a function of luminosity in various filters is presented in § 5, as well as our measurement of the baryon fraction in galaxies. Throughout the paper we adopt a flat cosmology with  $\Omega_m = 0.3$ ,  $\Omega_\Lambda = 0.7$ , and a Hubble parameter  $H_0 = 100 \text{ h km s}^{-1} \text{ Mpc}^{-1}$ .

## 2. DATA

The Red-Sequence Cluster Survey is a galaxy cluster survey designed to provide a large sample of optically selected clusters of galaxies in a large volume (see Gladders & Yee 2005 for a detailed discussion of the survey). To this end,  $92 \text{ deg}^2$  of the sky were imaged in both  $R_C$  and  $z'$  using the CFH12k camera on CFHT and the Mosaic II camera on the Cerro Tololo Inter-American Observatory (CTIO) Blanco telescope. This choice of filters allows for the detection of clusters up to  $z \sim 1.4$  using the cluster red-sequence method developed by Gladders & Yee (2000).

After completion of the original RCS survey, part of the surveyed area was imaged in both the  $B$  and  $V$  bands using the CFHT. This additional color information allows for a better selection of clusters at lower redshifts. These follow-up observations cover  $\sim 33.6 \text{ deg}^2$ , thus covering  $\sim 70\%$  of the CFHT fields. The data and the photometric reduction are described in detail in Hsieh et al. (2005).

The galaxy-galaxy lensing results presented in Hoekstra et al. (2004) were based on  $45.5 \text{ deg}^2$  of  $R_C$ -band data alone. The addition of  $B$  and  $V$  imaging data for  $33.6 \text{ deg}^2$  to the existing  $R_C$  and  $z'$  data allows for the determination of photometric redshifts for both lenses and sources in this subset of RCS imaging data. This enables the study of the lensing signal as a function of the photometric properties of the lens galaxies (i.e., color and luminosity). In this paper we focus on this multicolor subset of the RCS.

To determine the rest-frame  $B$ ,  $V$ , and  $R$  luminosities, we use template spectra for a range in spectral types and compute the corresponding passband corrections as a function of redshift and galaxy color (this procedure is similar to the one described in van Dokkum & Franx 1996). Provided the observed filters straddle the redshifted filter of interest, which is the case here, this procedure yields very accurate corrections.

The CFHT  $R_C$  images are used to measure the shapes of galaxies used in the weak-lensing analysis. The raw galaxy shapes are corrected for the effects of the point-spread function (PSF), as described in Hoekstra et al. (2002d). The resulting object cat-

alogs have been used for a range of weak-lensing studies (e.g., Hoekstra et al. 2002b, 2002c, 2002d, 2004) and we refer to these papers for a detailed discussion of the shape measurements.

The measurements of the lensing signal caused by large-scale structure presented in Hoekstra et al. (2002c, 2002d) are very sensitive to residual systematics. The various tests described in these papers suggest that the systematics are well under control. In this paper we use the shape measurements to measure the galaxy-galaxy lensing signal, which is much less sensitive to these observational distortions: in galaxy-galaxy lensing one measures the lensing signal that is perpendicular to the lines connecting many lens-source pairs. These are randomly oriented with respect to the PSF anisotropy, and therefore residual systematics are suppressed.

### 2.1. Photometric Redshift Distribution

The determination of the photometric redshifts is described in detail in Hsieh et al. (2005). The empirical quadratic polynomial fitting technique (Connolly et al. 1995) is used to estimate redshifts for the galaxies in the RCS data. The key component in this approach is the creation of a training set. Spectroscopic redshifts from the second Canadian Network for Observational Cosmology (CNOC2) survey (Yee et al. 2000) are matched to the corresponding objects in the overlapping RCS fields. These data are augmented with observations of the Great Observatories Origins Deep Survey/Hubble Deep Field–North (GOODS/HDF-N) field, for which the spectroscopic redshifts have been obtained using the Keck Telescope (Wirth et al. 2004; Cowie et al. 2004), and the photometry is from the ground-based Hawaii'i HDF-N data obtained with the Subaru Telescope (Capak et al. 2004). This results in a final training set that includes 4924 objects covering a large range in redshifts. To minimize the fitting errors arising from different galaxy types, Hsieh et al. (2005) used a  $kd$ -tree method with 32 cells in a three-dimensional color–color magnitude space.

The resulting catalog contains  $1.2 \times 10^6$  galaxies with photometric redshifts. This catalog was matched against the catalog of galaxies for which shapes were measured. This resulted in a sample of  $8 \times 10^5$  galaxies with  $18 < R_C < 24$  that are used in the analysis presented here.

Comparison with the spectroscopic redshifts shows that accurate photometric redshifts, with  $\sigma_z < 0.06$ , can be derived in the range  $0.2 < z < 0.5$ . At lower redshifts, the lack of  $U$ -band data limits the accuracy, whereas at higher redshifts photometric errors increase the scatter to  $\sigma_z \sim 0.12$  (see Hsieh et al. 2005 for more details).

To study the halos of galaxies as a function of color and luminosity, we select a sample of lenses at intermediate redshifts: we select galaxies with photometric redshifts  $0.2 < z < 0.4$  and  $R_C$ -band magnitudes  $18 < R_C < 24$ . This redshift range is well covered by the CNOC2 redshift survey at the bright end, and the redshift errors are relatively small. For the background galaxies we limit the analysis to galaxies with  $z_{\text{phot}} < 1$ .

Figure 1 shows the difference between spectroscopic and photometric redshifts for different subsets of galaxies with photometric redshifts  $0.2 < z < 0.4$ . Figure 1a shows the full sample, whereas Figures 1b and 1c show the bright and faint halves, respectively. The distribution is peaked, with 70% of the galaxies within the range  $|\Delta z| < 0.06$  (0.05 and 0.07 for the bright and faint subsets, respectively) and 90% within  $|\Delta z| < 0.12$  (0.085 and 0.15 for the bright and faint subsets, respectively).

The solid histogram in Figure 2a shows the normalized photometric redshift distribution for the galaxies brighter than

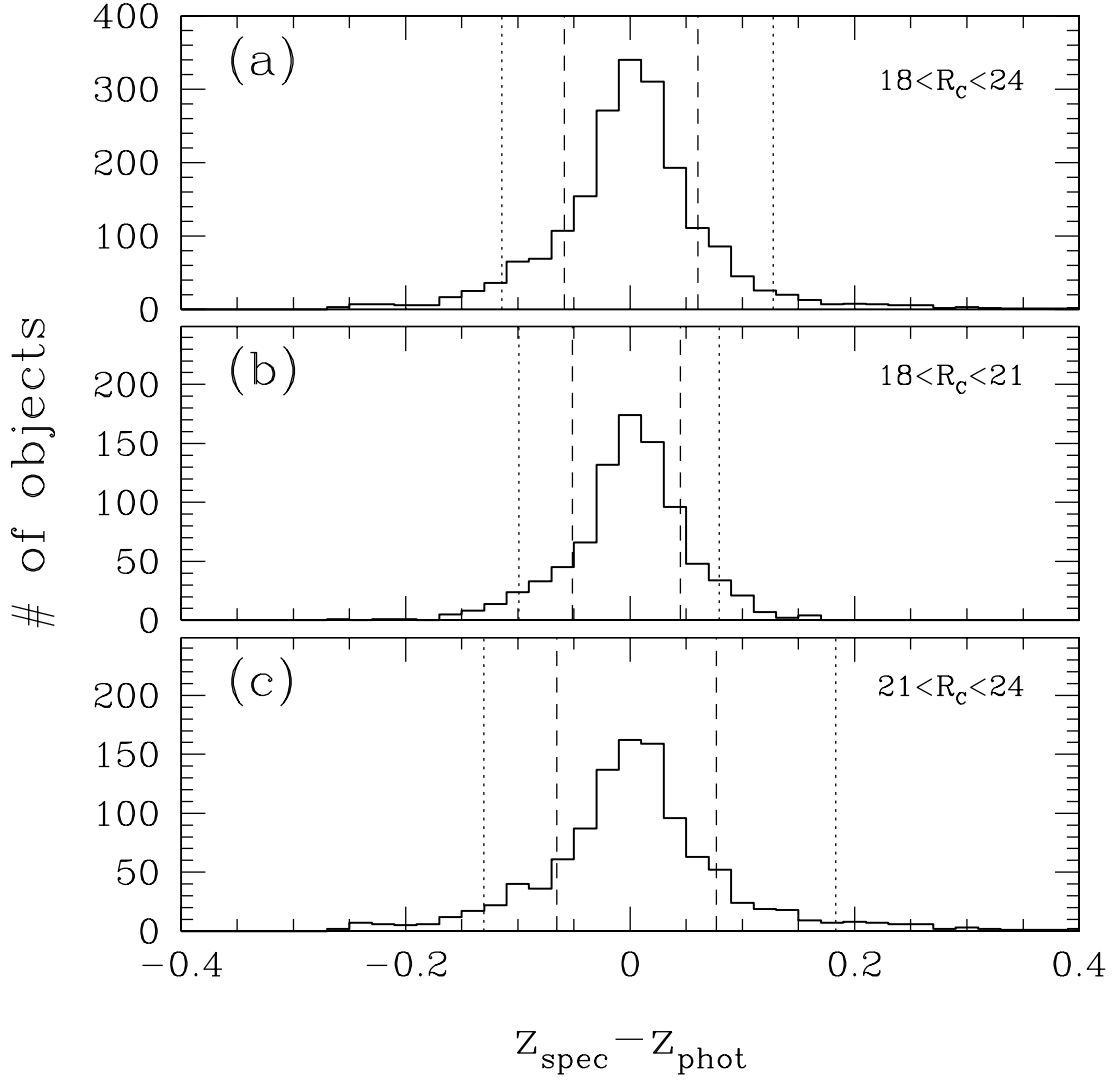


FIG. 1.—(a) Difference in spectroscopic and photometric redshifts for galaxies in the training set, with  $18 < R < 24$  and photometric redshifts  $0.2 < z_{\text{phot}} < 0.4$ . Our sample of lenses is selected to be in this redshift and magnitude range. The dotted lines indicate the intervals containing 90% of the galaxies, and the dashed lines indicate the 70% interval. (b) Same as (a), but for the brighter half of the training set; i.e., galaxies with  $18 < R < 21$ . (c) Same as (a), but for the galaxies with  $21 < R < 24$ , the fainter half of the lenses.

$R_c = 24$ . It is common to parametrize the redshift distribution, and a useful form is given by

$$p(z) = \frac{\beta}{z_s \Gamma[(1 + \alpha)/\beta]} \left(\frac{z}{z_s}\right)^\alpha \exp\left[-\left(\frac{z}{z_s}\right)^\beta\right]. \quad (1)$$

We fit this model to the observed redshift distribution. However, the uncertainties in the photometric redshift determinations can be substantial, and as a result the observed distribution is broadened. We use the observed error distribution, assuming a normal distribution, to account for the redshift errors. For the best-fit parameterization we find values of  $z_s = 0.29$ ,  $\alpha = 2$  (fixed), and  $\beta = 1.295$ , which yields a mean redshift of  $\langle z \rangle = 0.53$ . This model redshift distribution (which includes the smoothing by redshift errors) is indicated by the smooth curve in Figure 2a.

In the weak-lensing analysis, objects are weighted by the inverse square of the uncertainty in the shear measurement (e.g., see Hoekstra et al. 2000, 2002d). As more distant galaxies are fainter, they tend to have somewhat lower weights, and the effective redshift distribution is changed slightly. The dashed histo-

gram in Figure 2a shows the distribution weighted by the uncertainty in the shape measurement for each redshift bin. The best-fit parameterized redshift distribution has parameters  $z_s = 0.265$ ,  $\alpha = 2.2$  (fixed), and  $\beta = 1.30$ , which yield  $\langle z \rangle = 0.51$ , only slightly lower than the unweighted case.

## 2.2. Implications for Cosmic Shear Results?

Hoekstra et al. (2002c) presented constraints on the matter density  $\Omega_m$  and the normalization of the power spectrum  $\sigma_8$  by comparing CDM predictions to the observed lensing signal caused by large-scale structure. The derived value for  $\sigma_8$  depends critically on the adopted redshift distribution. Hoekstra et al. (2002c) used galaxies with  $22 < R_c < 24$  and a redshift distribution given by  $z_s = 0.302$ ,  $\alpha = 4.7$ , and  $\beta = 1.7$ , which yields a mean redshift of  $\langle z \rangle = 0.59$ . These parameters were based on a comparison with redshift distributions determined from the Hubble Deep Fields.

It is useful to examine how these assumptions compare to the RCS photometric redshift distribution for galaxies with  $22 < R_c < 24$ , as displayed in Figure 2b. The best-fit model, indicated by the smooth curve, has parameters  $z_s = 0.31$ ,  $\alpha = 3.50$ , and

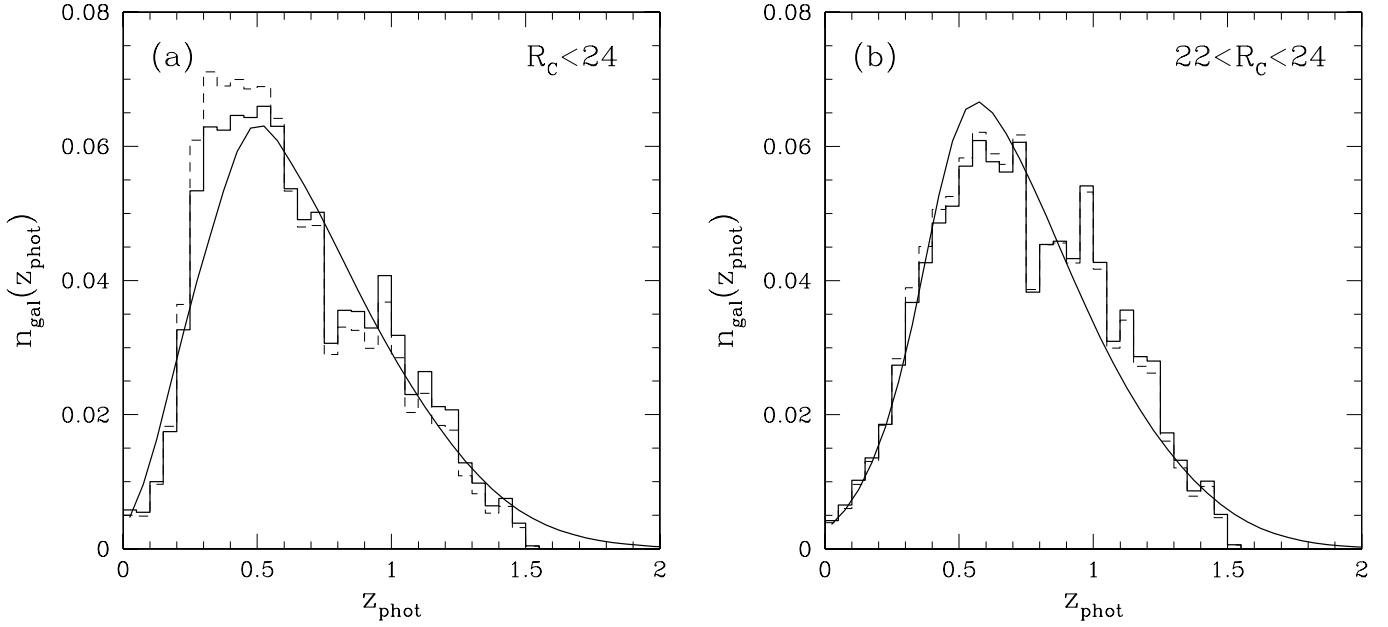


FIG. 2.—Plot of  $z_{\text{phot}}$  vs.  $n_{\text{gal}}$ . (a) The solid histogram shows the normalized photometric redshift distribution for the galaxies with redshifts and magnitudes  $R_c < 24$  that are included in the weak-lensing analysis. The solid smooth curve shows the best-fit model redshift distribution (see text for details). (b) Similar to (a), but for galaxies with  $22 < R_c < 24$ , corresponding to the range used by Hoekstra et al. (2002c). It is important to note that the lack of a relatively good training set for  $z > 0.6$  limits the interpretation. The dashed histogram shows the distributions weighted by the uncertainty in the shape measurement for each redshift bin. [See the electronic edition of the *Journal* for a color version of this figure.]

$\beta = 1.45$ , implying a mean redshift of 0.65, about 10% higher than that used by Hoekstra et al. (2002c). It is important to note, however, that the training set lacks a large number of objects beyond  $z = 0.8$  and  $R_c > 22$ . Despite these shortcomings, the mean redshift of sources appears higher than what was used in Hoekstra et al. (2002c), thus suggesting that their value for  $\sigma_8$  needs to be revised downward. The suggested change in source redshift could reduce the value for  $\sigma_8$  from Hoekstra et al. (2002c) by about 8% to  $\sigma_8 \sim 0.8$ . Unfortunately, it is not possible to robustly quantify the size of the revision. We stress that without further work on photometric redshifts for faint, high-redshift galaxies, it will be difficult to interpret current and, most importantly, future cosmic shear results.

The galaxy-galaxy lensing signal examined in this paper is much less sensitive to the uncertainty in the redshift distribution of faint, distant galaxies, as most of the signal is caused by lenses at much lower redshifts. As mentioned above, to further minimize uncertainties in our results, we only use background galaxies with redshifts less than 1 and select a sample of lenses with redshift  $0.2 < z < 0.4$ .

### 3. TESTING THE PHOTOMETRIC REDSHIFTS

Hsieh et al. (2005) present various tests of the accuracy of the photometric redshifts. Comparison to the available spectroscopic data, as well as comparing to other published distributions, provides a clear way to quantify the uncertainties. In this section we discuss some additional tests, based on the fact that the amplitude of the lensing signal is a well-known function of the source redshift. Such a test provides a useful “sanity” check on the validity of the photometric redshift distribution.

The azimuthally averaged tangential shear  $\langle \gamma_t \rangle$  as a function of distance from the lens is a useful measure of the lensing signal (e.g., Miralda-Escudé 1991):

$$\langle \gamma_t \rangle(r) = \frac{\bar{\Sigma}(<r) - \bar{\Sigma}(r)}{\Sigma_{\text{crit}}} = \bar{\kappa}(<r) - \bar{\kappa}(r), \quad (2)$$

where  $\bar{\Sigma}(<r)$  is the mean surface density within an aperture of radius  $r$  and  $\bar{\Sigma}(r)$  is the mean surface density on a circle of radius  $r$ . The convergence  $\kappa$ , or dimensionless surface density, is the ratio of the surface density and the critical surface density  $\Sigma_{\text{crit}}$ , which is given by

$$\Sigma_{\text{crit}} = \frac{c^2}{4\pi G} \frac{D_s}{D_l D_{ls}}, \quad (3)$$

where  $D_l$  is the angular diameter to the lens and  $D_s$  and  $D_{ls}$  are the angular diameter distances from the observer to the source and from the lens to the source, respectively. It is convenient to define the parameter

$$\beta = \max[0, D_{ls}/D_s], \quad (4)$$

which is a measure of how the amplitude of the lensing signal depends on the redshifts of the source galaxies. For instance, in the case of a singular isothermal sphere (SIS) model, the dimensionless surface density is

$$\kappa = \gamma_t = \frac{r_E}{2r}, \quad (5)$$

where  $r_E$  is the Einstein radius. Under the assumption of isotropic orbits and spherical symmetry, the Einstein radius (in radians) is related to the velocity dispersion and  $\beta$  through

$$r_E = 4\pi \left( \frac{\sigma}{c} \right)^2 \beta. \quad (6)$$

To test the photometric redshifts from the RCS, we use galaxies with photometric redshifts  $0.2 < z < 0.4$  to define a sample of lenses. We compute the ensemble-averaged tangential shear around these galaxies (i.e., the galaxy-mass cross-correlation function) as a function of source redshift. Brighter galaxies are expected to be more massive and should be given more weight. To derive

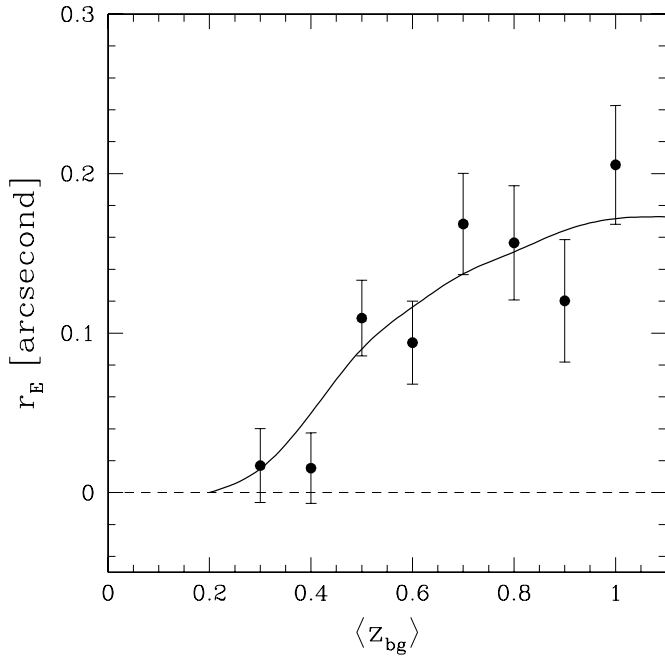


FIG. 3.—Best-fit Einstein radius obtained from a fit to the tangential shear as a function of the redshift of the background galaxies. Lenses were selected to have photometric redshifts in the range  $0.2 < z < 0.4$ . The solid line corresponds to the dependence of the lensing signal for a  $\Lambda$ CDM cosmology. The observed lensing signal scales with redshift as expected. [See the electronic edition of the Journal for a color version of this figure.]

the lensing signal, we assume that the velocity dispersion scales with luminosity as  $\sigma \propto L_B^{0.3}$ , a choice that is motivated by the observed slope of the  $B$ -band Tully-Fisher relation (e.g., Verheijen 2001).

We select bins with a width of 0.1 in redshift and measure the galaxy-mass cross-correlation function (e.g., see Hoekstra et al. 2004; Sheldon et al. 2004) out to  $10'$ . This signal arises from the combination of the clustering properties of the lenses and the underlying dark matter distribution. In the remainder of the paper, while studying the properties of dark matter halos around galaxies, we limit the analysis to smaller radii and to “isolated” lenses. However, by extending the range of measurements in this section, the signal-to-noise ratio is higher. The signal is well described by a SIS model for this range of scales (as suggested by the reduced  $\chi^2$  values for the fits). The resulting value for the Einstein radius as a function of redshift for the background galaxies is presented in Figure 3.

We find a negligible lensing signal for galaxies at the redshift of the lenses, whereas it increases for more distant sources. For a given cosmology and a pair of lens and source redshifts, the value of  $\beta$  can be readily computed. However, the errors in the photometric redshift determination complicate such a simple comparison between the expected signal and the results presented in Figure 3. As was the case for the photometric redshift distribution, the redshift errors change the signal. For instance, at low redshifts, higher redshift galaxies scatter into this bin, thus increasing the lensing signal. At higher redshifts, lower redshift objects scatter upward, lowering the signal.

When comparing the observed signal to the signal expected on the basis of the adopted  $\Lambda$ CDM cosmology, we must account for these redshift errors. To this end, we create simulated catalogs. The first step is to compute a model lensing signal based on the observed photometric redshifts (which are taken to be exact). We then create a mock catalog by adding the random errors

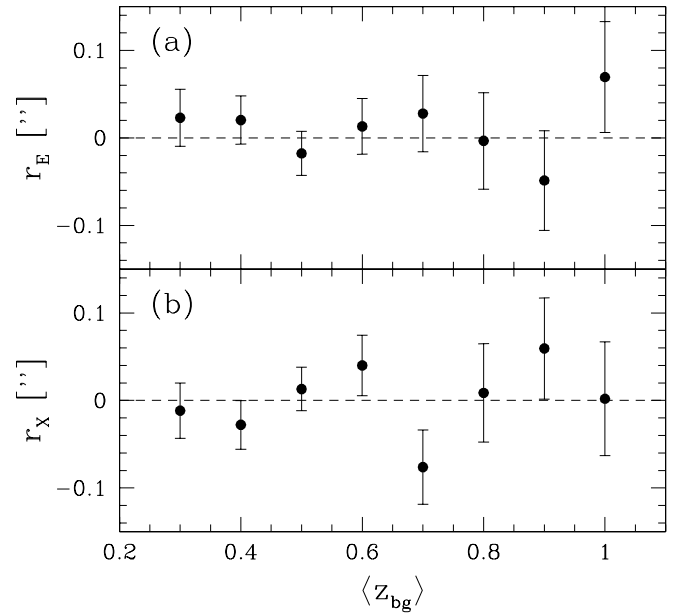


FIG. 4.—(a) Best-fit Einstein radius obtained from a fit to the tangential shear when the lenses and sources are selected to be in the same redshift bin. In this case, no signal should be present, in agreement with the measurements. This result also indicates that intrinsic tangential alignments are negligible. (b) Results when the background galaxies are rotated by  $45^\circ$  (B mode). In this case also, no signal is detected.

to the redshift (while leaving the lensing signal unchanged). These random errors are based on the observed distribution (see, e.g., Fig. 1). We measure the lensing signal as a function of redshift in the mock catalog. This signal, indicated by the solid line in Figure 3, can be compared directly to our actual measurements, as it now includes the smoothing effect of redshift errors. Figure 3 shows that it traces the observed change in the amplitude of the lensing signal very well.

Another useful experiment is to measure the lensing signal when the lenses and sources are in the same redshift bin. We note that this procedure enhances the probability that we measure the signal for galaxies that are physically associated. If satellite galaxies tend to be aligned tangentially or radially, this would also lead to a positive or negative signal, respectively. The results from Bernstein & Norberg (2002), based on an analysis employing spectroscopic redshifts, have shown that intrinsic tangential alignments are negligible. Unfortunately, in our case, the much larger photometric redshift errors (compared to spectroscopic redshifts) effectively suppress this potentially interesting signal. In addition, for the RCS data, the interpretation of the signal requires a large set of spectroscopic redshifts to quantify the contributions of unassociated galaxies in each bin.

Instead, we use these measurements as a test of the photometric redshifts. The results are presented in Figure 4. Figure 4a shows the results for the tangential shear, whereas Figure 4b shows the results when the background galaxies are rotated by  $45^\circ$  (which is a measure of systematics). In both cases, we do not observe a significant signal. The lack of a signal in the tangential shear in this case implies that the errors in photometric redshifts are relatively small. If this were not the case, and higher redshift galaxies would contaminate the samples at lower redshifts, we would expect to observe a positive signal.

#### 4. GALAXY DARK MATTER PROFILE

One of the major advantages of weak gravitational lensing over dynamical methods is that the lensing signal can be measured out

to large projected distances from the lens. However, at large radii, the contribution from a particular galaxy may be small compared to its surroundings: a simple interpretation of the measurements can only be made for isolated galaxies.

In practice, galaxies are not isolated, which is particularly true for bright, early-type galaxies. In their analysis of SDSS data, Guzik & Seljak (2002) quantified the contribution from clustered galaxies using a halo model approach. As discussed in § 5, we follow a different approach by selecting relatively isolated galaxies. As a result, our results are not strictly valid for the galaxy population as a whole. Nevertheless, the selection procedure is well defined and can be readily implemented when comparing to numerical simulations.

We limit the analysis to relatively small distances from the lens, thus ensuring that the signal is dominated by the lens itself. As a result, we need to adopt a model for the mass distribution to relate the lensing signal to the mass of the lens. Our choice is motivated by the results of CDM simulations.

Collisionless CDM provides a good description for the observed structures in the universe. Numerical simulations, which provide a powerful way to study the formation of structure in the universe, indicate that on large scales CDM gives rise to a particular density profile (e.g., Dubinski & Carlberg 1991; Navarro et al. 1995, 1996, 1997; Moore et al. 1999). We note, however, that there are still uncertainties regarding the slope at small radii and the best analytical description of the profile (e.g., Moore et al. 1999; Diemand et al. 2004; Hayashi et al. 2004; Tasitsiomi et al. 2004a). Furthermore, there is considerable scatter from halo to halo in the simulations. Our observations, however, cannot distinguish between these various profiles, and instead we focus on the commonly used Navarro-Frenk-White (NFW) profile, given by

$$\rho(r) = \frac{M_{\text{vir}}}{4\pi f(c) r(r+r_s)^2}, \quad (7)$$

where  $M_{\text{vir}}$  is the virial mass, which is the mass enclosed within the virial radius  $r_{\text{vir}}$ . The virial radius is related to the “scale radius”  $r_s$  through the concentration  $c = r_{\text{vir}}/r_s$ . The function  $f(c) = \ln(1+c) - c/(1+c)$ .

One can fit the NFW profile to the measurements with  $M_{\text{vir}}$  and concentration  $c$  (or, equivalently,  $r_s$ ) as free parameters. However, numerical simulations have shown that the average concentration depends on the halo mass and the redshift. Hoekstra et al. (2004) constrained the mass and scale radius of the NFW model using a maximum likelihood analysis of the galaxy-galaxy lensing signal and found that the results agreed well with the predictions from simulations. We therefore adopt the results from Bullock et al. (2001), who found from simulations that

$$c = \frac{9}{1+z} \left( \frac{M_{\text{vir}}}{8.12 \times 10^{12} h M_{\odot}} \right)^{-0.14}. \quad (8)$$

It is good to note that individual halos in the simulations have a lognormal dispersion of approximately 0.14 around the median. For the virial mass estimates presented here, we use this relation between mass and concentration, thus assuming that we can describe the galaxy mass distribution by a single parameter.

By definition, the virial mass and radius are related by

$$M_{\text{vir}} = \frac{4\pi}{3} \Delta_{\text{vir}}(z) \rho_{\text{bg}}(z) r_{\text{vir}}^3, \quad (9)$$

where  $\rho_{\text{bg}} = 3H_0^2 \Omega_m(1+z)^3/(8\pi G)$  is the mean density at the cluster redshift and the virial overdensity  $\Delta_{\text{vir}} \approx (18\pi^2 + 82\xi -$

$39\xi^2)/\Omega(z)$ , with  $\xi = \Omega(z) - 1$  (Bryan & Norman 1998). For the  $\Lambda$ CDM cosmology considered here,  $\Delta_{\text{vir}}(0) = 337$ . We also note that for the adopted  $\Lambda$ CDM cosmology, the virial mass is different from the widely used  $M_{200}$ . This mass is commonly defined as the mass contained within the radius  $r_{200}$ , where the mean mass density of the halo is equal to  $200\rho_c$  (i.e., setting  $\Delta = 200$  and  $\rho_{\text{bg}} = \rho_c$  in eq. [9]). Note, however, that other definitions for  $M_{200}$  can be found in the literature as well. The expressions for the tangential shear and surface density for the NFW profile have been derived by Bartelmann (1996) and Wright & Brainerd (2000), and we refer the interested reader to these papers for the relevant equations.

## 5. RESULTS

As discussed above, we study a sample of lenses with photometric redshifts  $0.2 < z < 0.4$  and  $18 < R_C < 24$ . This first selection yields  $\sim 1.4 \times 10^5$  lenses. We split this sample in a number of luminosity and color bins and determine the virial radii from an NFW model fit to the observed lensing signal.

For bright galaxies the lensing signal on small scales is typically dominated by the dark matter halo associated with that galaxy. In the case of faint (low mass) galaxies, however, the signal can easily be dominated by contributions from a massive neighbor. Note that this neighbor need not be physically associated with the lens, as all matter along the line of sight contributes to the lensing signal.

We can study the relevance of the local (projected) density by measuring the lensing signal around a sample of “faint” lenses ( $10^9 h^{-2} L_{B,\odot} < L_B < 5 \times 10^9 h^{-2} L_{B,\odot}$ ) as a function of the projected distance to the nearest “bright” lens ( $L_B > 5 \times 10^9 h^{-2} L_{B,\odot}$ ). This distance can be used as a crude measure of the density around the faint lens (i.e., the smaller the distance, the higher the density).

To this end, we split this sample of faint lenses into subsets on the basis of their distance to the nearest bright galaxy. We fit a SIS model to the ensemble-averaged lensing signal out to  $2'$  ( $\sim 400 h^{-1}$  kpc at the mean distance of the lenses) for each bin. The reduced  $\chi^2$  values for the best fit are all close to unity, indicating that the SIS model provides a good fit to these observations. We found that limiting the fit to smaller radii did not change the results, apart from increasing the measurement errors. Figure 5 shows the derived value for the Einstein radius as a function of the distance to the nearest bright galaxy.

The results show a clear increase in lensing signal as the separation decreases; i.e., as the density increases. However, at separations larger than  $\sim 30''$ , the observed lensing signal appears to be independent of the density. Larger data sets are required to make more definitive statements, but these findings suggest that we can measure the properties of isolated faint galaxies by limiting the sample to galaxies that are more than  $30''$  away from a brighter galaxy. Although this is a rather strict selection for the faintest galaxies, bright galaxies can be surrounded by many faint galaxies and consequently are not truly isolated. In the remainder of this paper, we present results based on the sample of “isolated” galaxies, unless specified otherwise. This selection reduces the sample of lenses to 94,509 galaxies.

### 5.1. Mass-Luminosity Relation

We split the sample of isolated lens galaxies into seven luminosity bins and measure the mean tangential distortion as a function of radius out to  $2'$ . We fit an NFW profile to these measurements, with the virial mass as a free parameter, as described in § 4.

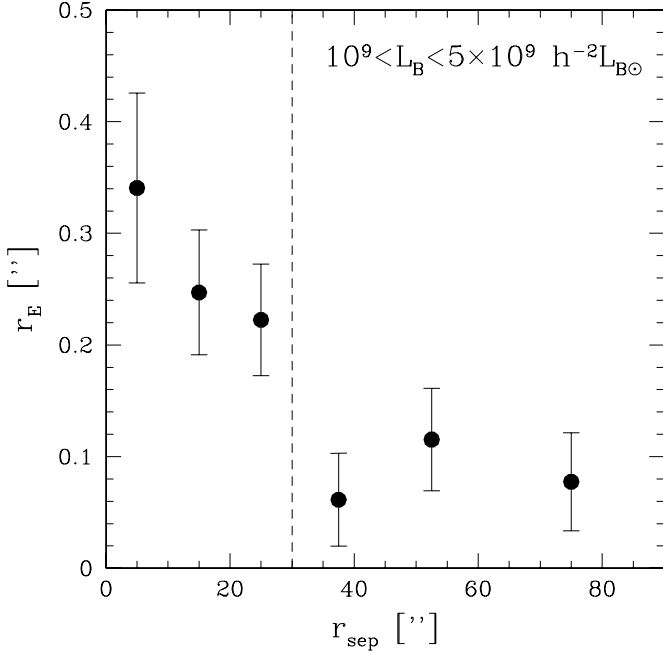


FIG. 5.—Einstein radius for faint lenses as a function of projected distance to the nearest bright lens,  $r_{\text{sep}}$ . The faint galaxies have luminosities  $10^9 h^{-2} L_{B,\odot} < L_B < 5 \times 10^9 h^{-2} L_{B,\odot}$ , whereas the bright galaxies have  $L_B > 5 \times 10^9 h^{-2} L_{B,\odot}$ .

Figure 6 shows the measurements of the tangential shear as a function of projected distance from the lens for the seven  $R$ -band luminosity bins. The results for the  $B$  and  $V$  filters are very similar to the ones presented in Figure 6. To account for the fact that the lenses span a range in redshift, we have scaled the signal such that it corresponds to that of a lens at the mean lens redshift ( $z \sim 0.32$ ) and a background galaxy at infinite redshift. In each panel in Figure 6, the average rest-frame  $R$ -band luminosity for each bin is indicated (in units of  $10^9 h^{-2} L_{R,\odot}$ ). The vertical scales in each of the panels in Figure 6 are the same, and as the lumi-

nosity of the lenses increases, we observe a clear increase in the strength of the lensing signal. The best-fit NFW models for each bin are indicated by the dotted curves. Note that the current observations cannot distinguish between an NFW profile (used here) and other profiles, such as the SIS model.

There are more faint galaxies than bright galaxies, and the errors in the photometric redshift estimates will have the net effect of faint galaxies getting scattered to higher luminosity bins, hence biasing the mass at a fixed luminosity to a lower value. To estimate the level of this bias, we create mock catalogs. We assume a power-law mass-luminosity relation and compute the model lensing signal using the observed photometric redshifts of the lens and source galaxies. We analyze this “perfect” catalog and compute the virial masses as a function of luminosity. We then use the observed photometric redshift error distribution as a function of apparent magnitude (see Fig. 1) to create a number of new catalogs where the random error is added to the redshift (note that the lensing signal is not changed). These catalogs are also analyzed and yield the “observed” virial mass as a function of luminosity.

As expected, the resulting masses are smaller than the input masses and the change in mass depends on the luminosity. The results are presented in Figure 7 for the  $B$ ,  $V$ , and  $R$  bands. Different choices for the mass-luminosity relation (within reasonable bounds) yield very similar curves. To infer the correct virial mass, we scale the observed virial masses by these curves.

At the low-luminosity end, the corrections are large because of the relatively large errors in redshift. At the bright end, however, the redshift errors are smaller, but the number of bright galaxies decreases rapidly (because of the shape of the luminosity function), and a relatively larger fraction of intrinsically lower mass systems ends up in the high-luminosity bin, resulting in an increase of the correction factor. The corrections are substantial at both ends, but the origin is well understood, and the associated uncertainty is small.

The corrected virial masses as a function of luminosity in the  $B$ ,  $V$ , and  $R$  bands are presented in Figure 8 (*top*), and the best-fit

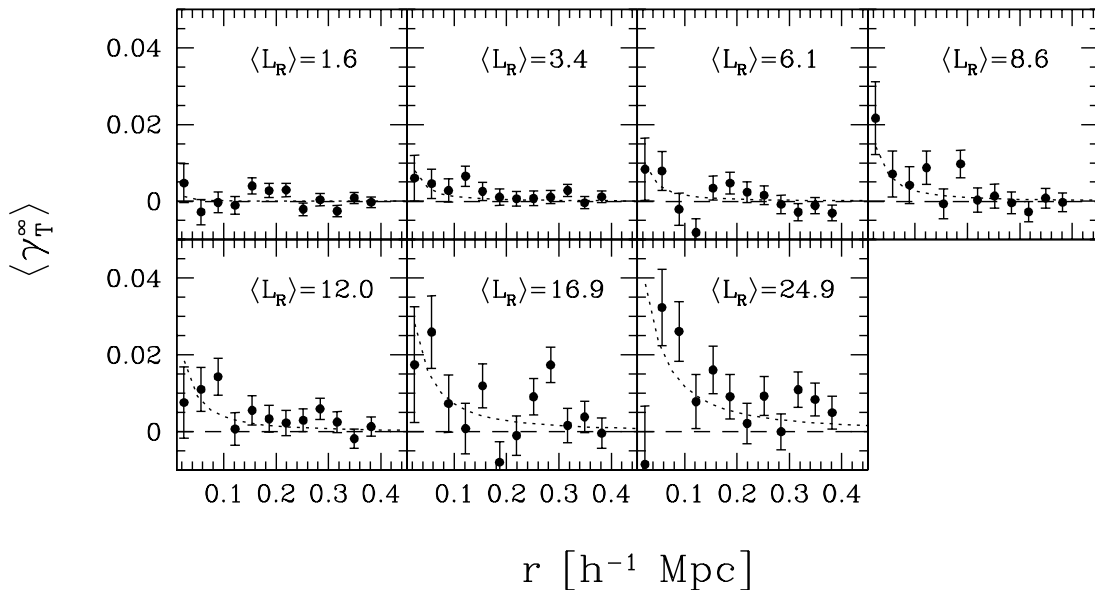


FIG. 6.—Tangential shear as a function of projected (physical) distance from the lens for each of the seven rest-frame  $R$ -band luminosity bins. To account for the fact that the lenses have a range in redshifts, the signal is scaled such that it corresponds to that of a lens at the average lens redshift ( $z \sim 0.32$ ) and a source redshift of infinity. The mean rest-frame  $R$ -band luminosity for each bin is also shown in the figure in units of  $10^9 h^{-2} L_{R,\odot}$ . The strength of the lensing signal clearly increases with increasing luminosity of the lens. The dotted line indicates the best-fit NFW model to the data. The tangential shear profiles for the  $B$  and  $V$  bands are very similar, and we only present the final results for the  $R$  filter in Fig. 8.

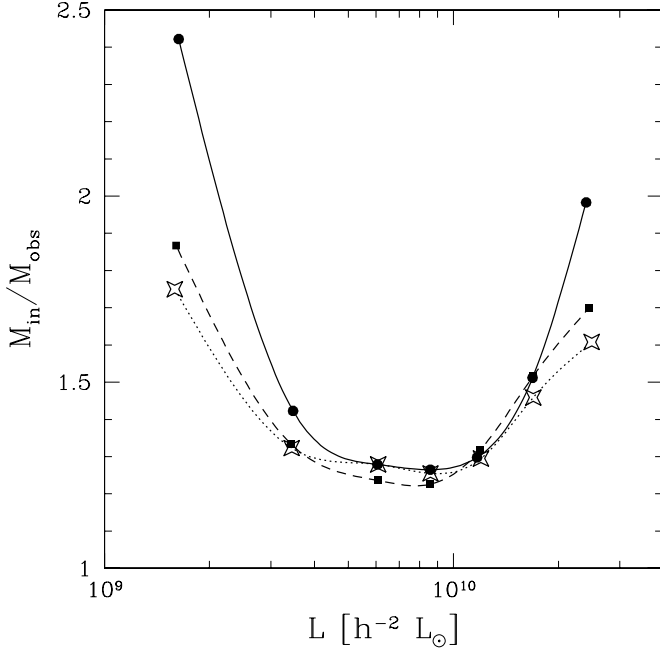


FIG. 7.—Ratio of the input virial mass and the observed mass after adding photometric redshift errors. The dependence with luminosity is dominated by how the redshift errors depend on brightness. The resulting curves depend only very weakly on the input mass-luminosity relation. The corrections are somewhat different for the various rest-frame bands. The solid line with filled circles corresponds to the *B*-band results, the dashed line with filled squares shows the *V*-band results, and the dotted line with stars shows the *R*-band data. To infer the correct virial mass, we scale the observed virial masses by these curves.

virial masses are listed in Table 1. In all cases we see a clear increase of the virial mass with luminosity. The results suggest a power-law relation between the luminosity and the virial mass, although this assumption might not hold at the low-luminosity end (e.g., see Fig. 8, *bottom*). We therefore fit

$$M = M_{\text{fid}} \left( \frac{L}{10^{10} h^{-2} L_{\odot}} \right)^{\alpha} \quad (10)$$

to the measurements, where  $M_{\text{fid}}$  is the virial mass of a fiducial galaxy of luminosity  $L = 10^{10} h^{-2} L_{\odot}$ , where  $x$  indicates the relevant filter. The best fit in each filter is indicated by the dashed line in Figure 8. The resulting best-fit parameters for this mass-luminosity relation are listed in Table 2. We do not observe a change in the slope  $\alpha$  for the different filters, but we find that  $M_{\text{fid}}$  is decreasing for redder passbands.

Tasitsiomi et al. (2004b) studied the weak-lensing mass-luminosity relation from their numerical simulations. This study shows that the interpretation of the mass-luminosity relation presented in Figure 8 is complicated by the fact that the halos of galaxies of a given luminosity show a scatter in their virial masses. For the model adopted in Tasitsiomi et al. (2004b), the best-fit virial mass gives a value between the median and mean mass. The amplitude of this bias depends on the assumed intrinsic scatter in the mass-luminosity relation, which requires further study. The Tasitsiomi et al. (2004b) results imply that our results underestimate the actual mean virial mass but that the slope of the mass-luminosity relation is not changed.

Guzik & Seljak (2002) measured the mass-luminosity relation using data from the SDSS. The average luminosity of their sample of lenses is higher than that studied here. Also, the analysis

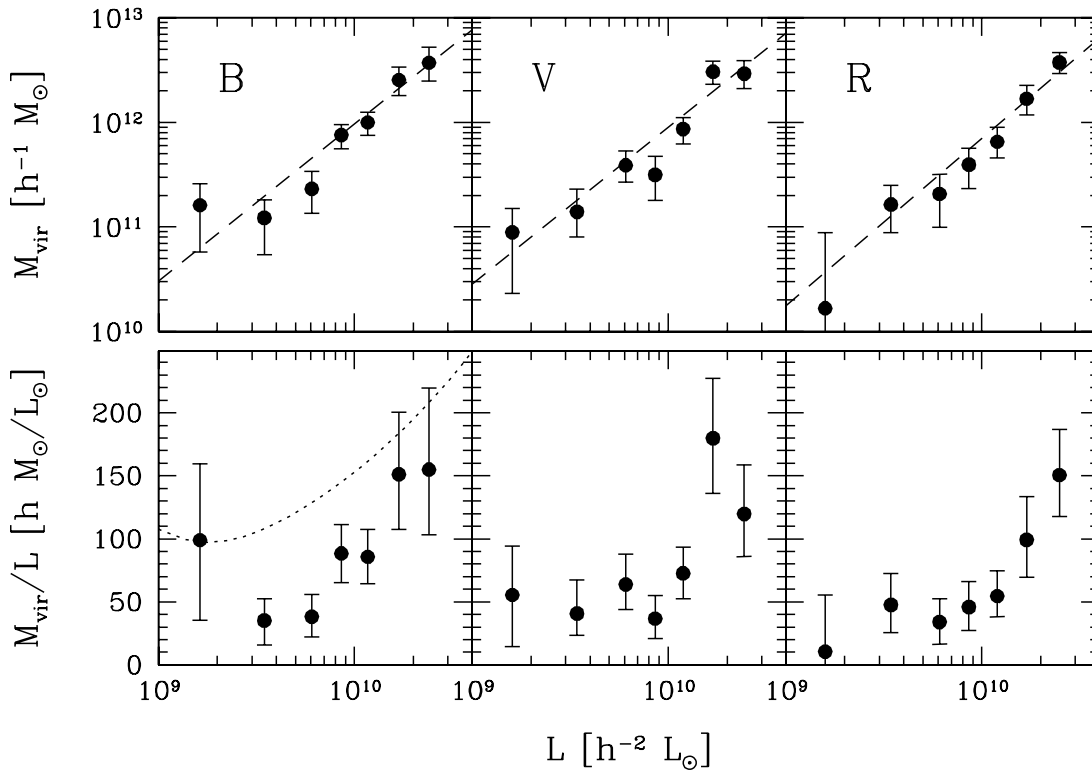


FIG. 8.—*Top*: Virial mass as a function of the rest-frame luminosity in the indicated filter. The dashed line indicates the best-fit power-law model for the mass-luminosity relation, with the relevant parameters listed in Table 2. *Bottom*: Observed rest-frame virial mass-to-light ratios. The results suggest a rise in the mass-to-light ratio with increasing luminosity, albeit with low significance. The dotted line in the panel showing the *B*-band mass-to-light ratio corresponds to model A from van den Bosch et al. (2003). It matches the observed dependence of the mass-to-light ratio with luminosity, but with an offset toward higher values.



TABLE 1  
BEST-FIT VIRIAL MASSES

$L_B$ ( $10^9 h^{-2} L_\odot$ )	$M_{\text{vir}}$ ( $10^{11} h^{-1} M_\odot$ )	$L_V$ ( $10^9 h^{-2} L_\odot$ )	$M_{\text{vir}}$ ( $10^{11} h^{-1} M_\odot$ )	$L_R$ ( $10^9 h^{-2} L_\odot$ )	$M_{\text{vir}}$ ( $10^{11} h^{-1} M_\odot$ )
1.6	$0.66^{+0.41}_{-0.43}$	1.6	$0.48^{+0.33}_{-0.35}$	1.6	$0.10^{+0.40}_{-0.30}$
3.5	$0.86^{+0.42}_{-0.48}$	3.4	$1.05^{+0.69}_{-0.45}$	3.4	$1.24^{+0.65}_{-0.57}$
6.1	$1.81^{+0.84}_{-0.75}$	6.1	$3.1^{+1.2}_{-1.0}$	6.1	$1.62^{+0.88}_{-0.84}$
8.6	$6.0^{+1.6}_{-1.6}$	8.6	$2.6^{+1.3}_{-1.1}$	8.6	$3.1^{+1.4}_{-1.3}$
11.7	$7.7^{+2.0}_{-1.9}$	11.9	$6.6^{+1.9}_{-1.8}$	12.0	$5.0^{+1.9}_{-1.5}$
16.9	$16.9^{+5.5}_{-4.9}$	17.0	$20.1^{+5.3}_{-4.9}$	16.9	$11.5^{+4.0}_{-3.4}$
24.0	$18.8^{+7.8}_{-6.3}$	24.5	$17.2^{+5.6}_{-4.9}$	24.9	$23.3^{+5.6}_{-5.1}$

NOTES.—Best-fit virial masses as a function of luminosity in the rest-frame  $B$ ,  $V$ , and  $R$  bands. The corresponding values for the concentration  $c$  can be computed with eq. (8), using a redshift of  $z = 0.32$  for the lenses. The listed errors indicate the 68% confidence limits.

by Guzik & Seljak (2002) differs from ours, as they model the contribution from other halos. Using the halo model approach, they compute the contributions of other halos to the lensing signal around a galaxy, including that of smooth group or cluster halos. In this paper, we have instead minimized such contributions to the galaxy-galaxy lensing signal by selecting “isolated” galaxies and limiting the analysis to the lensing signal within  $400 h^{-1}$  kpc from the lens. The results presented in Figures 5 and 6 suggest that this approach has worked well.

Guzik & Seljak (2002) present results for two different cases of group halo contributions. Depending on the assumed relative importance of such a halo, the derived mass changes only slightly. The assumptions for the halo contribution do affect the inferred slopes somewhat, although the change is small for the redder filters. Minimizing the halo contribution yields a power-law slope of  $\sim 1.5$ – $1.7$ , in excellent agreement with the findings presented here. However, when maximizing the effect, the slope decreases to  $\sim 1.3$ – $1.4$  in the red filters and to  $1.2 \pm 0.2$  in the  $g'$  band. It should be noted that the latter scenario is rather extreme, given that, with the exception of the central galaxy, the relative importance of the group halo is expected to diminish with increasing luminosity (i.e., mass) of the lens. In addition, the different range in luminosities probed in the two studies would most likely affect the results in the bluest filters.

Benson et al. (2000) present predictions for the  $B$ -band mass-luminosity relation based on semianalytic models of galaxy formation. In the luminosity range probed here, they obtain a power-law slope of  $\sim 1.6$ . Van den Bosch et al. (2003) used the conditional luminosity functions computed from the Two Degree Field (2dF) Galaxy Redshift Survey to constrain the variation of the mass-to-light ratio as a function of mass. Van den Bosch et al. consider a number of models, which provide similar mass-luminosity relations for the range of masses probed in this paper. We con-

sider their model A, which is obtained by fitting the data without constraining the model parameters. For this model the mass-luminosity relation is close to a power law with a slope of 1.3. Hence, both model predictions are in good agreement with our findings and the results of Guzik & Seljak (2002).

The agreement in the slope of the mass-luminosity relation strengthens the conclusion by Guzik & Seljak (2002) that rotation curves must decline substantially from the optical to the virial radius in order to reconcile our results with the observed scaling relations at small radii, such as the Tully-Fisher relation. A decrease in rotation velocity is also predicted by semianalytic models of galaxy formation (e.g., Kauffmann et al. 1999; Benson et al. 2000).

Guzik & Seljak (2002) define the virial mass in terms of an overdensity of 200 times the critical density, which is different from ours. They find a mass  $M_{200} = (9.3 \pm 1.6) \times 10^{11} h^{-1} M_\odot$  for a galaxy with a luminosity of  $1.1 \times 10^{10} h^{-2} h M_\odot / L_{g',\odot}$  at a redshift of  $z \sim 0.16$ . We convert our mass estimate to their definition and use the transformations between filters from Fukugita et al. (1996) to relate our results to those of Guzik & Seljak (2002). Furthermore, we assume that the fiducial galaxy is about 10% brighter at  $z = 0.32$ , compared to  $z = 0.16$ . Under these assumptions, our results translate to a mass of  $M_{200} = (11.7 \pm 1.7) \times 10^{11} h^{-1} M_\odot$  for a galaxy with a luminosity of  $1.1 \times 10^{10} h^{-2} h M_\odot / L_{g',\odot}$ , which is in agreement with the findings of Guzik & Seljak (2002) at the  $1 \sigma$  level.

Figure 8 (*bottom*) shows the inferred rest-frame mass-to-light ratios as a function of luminosity for the different filters. The results suggest a rise in mass-to-light ratio for galaxies more luminous than  $\sim 10^{10} h^{-2} L_\odot$  and little variation for fainter galaxies. This suggests that a power law is not sufficient to describe the mass-luminosity relation over the range probed here. However, a larger data set is needed to make a firm statement. The dashed curve in Figure 8 shows the values corresponding to model A from van den Bosch et al. (2003), converted to the  $B$  band and our definition of the virial mass. The predicted mass-to-light ratio is significantly higher compared to our measurements. This could point to a systematic underestimate of the virial masses from lensing due to scatter in the mass-luminosity relation, as suggested by Tasitsiomi et al. (2004b). Nevertheless, the model predictions are in qualitative agreement with the results presented in Figure 8, in the sense that they predict an increase for bright galaxies and a small increase in mass-to-light ratio toward lower luminosities.

TABLE 2  
BEST-FIT PARAMETERS OF THE MASS-LUMINOSITY RELATION

Filter (1)	$M_{\text{fid}}$ ( $10^{11} h^{-1} M_\odot$ ) (2)	$\alpha$ (3)
$B$ .....	$9.9^{+1.5}_{-1.3}$	$1.5 \pm 0.3$
$V$ .....	$9.3^{+1.4}_{-1.3}$	$1.5 \pm 0.2$
$R$ .....	$7.5^{+1.2}_{-1.1}$	$1.6 \pm 0.2$

NOTES.—Col. (2) lists the virial mass for a galaxy of luminosity  $10^{10} h^{-2} L_\odot$  in the indicated filter. Col. (3) lists the best-fit power-law slope of the mass-luminosity relation. The listed errors indicate the 68% confidence limits.

## 5.2. Star Formation Efficiency

In § 5.1 we studied the dependence of the mass-to-light ratio as a function of luminosity. The results suggest an increase for

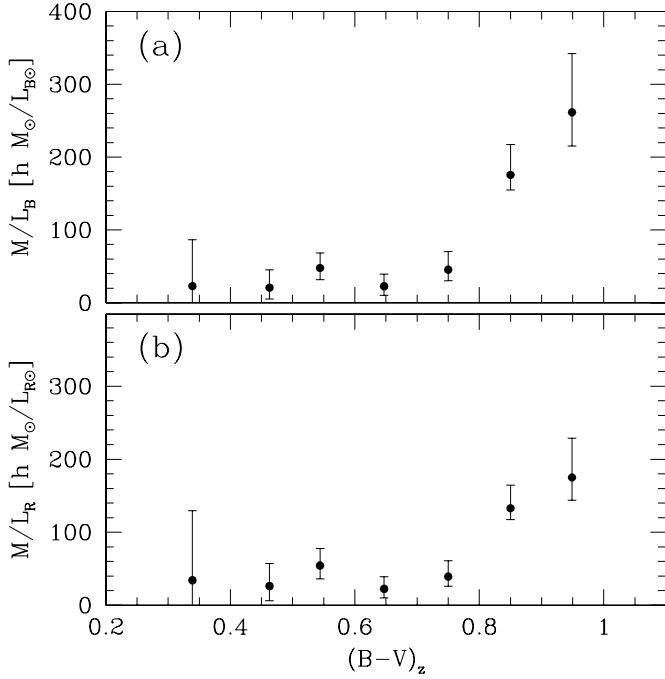


FIG. 9.—(a) Rest-frame  $B$ -band virial mass-to-light ratio as a function of rest-frame  $B - V$  color. (b) Same as (a), but for the rest-frame  $R$  band. In this case the change for the red galaxies is smaller. The filled circles represent the measurements for our sample of lenses, which have a mean redshift of  $z = 0.32$ .

luminous galaxies. A simple interpretation of these results, however, is complicated because the mix of galaxy type is also a function of luminosity. The more luminous galaxies are likely to be early-type galaxies rather than spiral galaxies.

Although we have not classified our sample of lenses, we can use the  $B - V$  color as a fair indicator of galaxy type (e.g., Roberts & Haynes 1994). Furthermore, the color can be used to estimate the mean stellar mass-to-light ratio, which also is a strong function of color (e.g., Bell & de Jong 2001). Comparison of the virial and stellar mass-to-light ratios then enables us to estimate the relative fraction of the mass that has been transformed into stars.

Figure 9a shows the inferred  $B$ -band mass-to-light ratio as a function of rest-frame  $B - V$  color. Figure 9a shows a clear increase in mass-to-light ratios for early-type galaxies, which have colors redder than  $\sim 0.8$ . It is useful to note that our selection of lenses allows for the brightest galaxies in the centers of denser regions to be included. Our simulations show that the inferred masses are not biased, but these tests do not include the smooth contributions from group halos. The resulting mass-to-light ratios are comparable to those determined for rich clusters of galaxies (e.g., Hoekstra et al. 2002a) and massive galaxy groups (Parker et al. 2005). For galaxies with  $B - V < 0.8$ , the mass-to-light ratio does not show a clear change with color, and we find an average mass-to-light ratio of  $M/L_B = 32 \pm 9 h M_\odot/L_{B,\odot}$ . Figure 9b shows the results for the  $R$ -band mass-to-light ratio. For galaxies with  $B - V < 0.8$ , we obtain an average value of  $M/L_R = 34 \pm 9 h M_\odot/L_{R,\odot}$ . The increase in mass-to-light ratio for red galaxies is smaller in the  $R$  band, which is expected since the stellar mass-to-light ratios also vary less.

As discussed in § 5.1, the measurements presented in Figure 9 are for a sample of galaxies with an average redshift of  $z = 0.32$ . Note that to compare these results to measurements at lower redshifts, one needs to account for evolution in both the colors and the luminosities of the lens galaxies. To this end we use

population synthesis models (e.g., Fioc & Rocca-Volmerange 1997) that indicate that the galaxies become redder as they age and that the reddest galaxies dim somewhat faster than the blue galaxies.

As mentioned above, it is interesting to estimate the fraction of mass in stars. To do so, we need to relate the luminosity to the stellar mass. Direct measurements of the stellar mass-to-light ratios are difficult, although rotation curves can provide useful limits on the maximum allowed value. Instead we rely on galaxy evolution models, which use evolutionary tracks and assumptions about the initial mass function (IMF), the star formation history, and feedback to compute stellar populations as a function of age.

There are many obvious difficulties in such work, given the complicated history of galaxies and the uncertainty in the IMF. The latter is of particular importance and gives rise to a relatively large uncertainty in the estimates, as we discuss below. Nevertheless, the dependence of the stellar mass-to-light ratio with color is fairly well constrained.

Bell & de Jong (2001) used a suite of galaxy evolution models to show that one expects substantial variation in stellar mass-to-light ratio as a function of galaxy color. Although their work focused on the properties of spiral galaxies, comparison with results for early-type galaxies suggests that we can extend their calculation to these galaxies as well. Bell & de Jong (2001) find that the models are well described by a linear relation between  $\log M/L$  and  $B - V$  color and provide tables with the slope and intercept of these relations. Their results, however, are for  $z = 0$ , but we have converted their results to the mean redshift of our lenses ( $z = 0.32$ ) using predictions based on the PEGASE code (Fioc & Rocca-Volmerange 1997), provided by D. Le Borgne. Compared to the results from  $z = 0$ , the galaxies are slightly bluer, with stellar mass-to-light ratios  $\sim 25\%$  lower at  $z = 0.32$ .

The resulting stellar mass-to-light ratio is most sensitive to the assumed IMF, and we consider two “extreme” cases, such that our results should bracket the real properties of galaxies. The first IMF we consider is the one proposed by Salpeter (1955). The  $z = 0.32$  stellar mass-to-light ratios based on the PEGASE code by Fioc & Rocca-Volmerange (1997) are presented in Figure 10 (bottom left) for the  $B$  band (solid line) and the  $R$  band (dashed line). As noted by Bell & de Jong (2001), a standard Salpeter (1955) IMF results in mass-to-light ratios that are too high to fit rotation curves of spiral galaxies. Hence, this model can be considered extreme in the sense that it provides a high estimate for the mass in stars. Instead, Bell & de Jong (2001) propose a scaled Salpeter IMF, which is equivalent to reducing the number of low-mass stars (which contribute to the mass, but not to the luminosity). We use the parameters from their Table 1. The results for this IMF, which fits the rotation curve data better, are shown in Figure 10 (bottom right).

We use these model stellar mass-to-light ratios to calculate the ratio  $M_{\text{vir}}/M_*$  as a function of color in both the  $B$  and  $R$  bands. The results are also presented in Figure 10. For a given model, the results between the two filters agree very well, and the average ratios are listed in Table 3 for a Hubble parameter of  $H_0 = 71 \text{ km s}^{-1} \text{ Mpc}^{-1}$ . However, the two models yield significantly different ratios.

Observations of the cosmic microwave background (CMB; e.g., Spergel et al. 2003) have yielded accurate measurements of the baryon fraction in the universe. On the basis of *Wilkinson Microwave Anisotropy Probe* (WMAP) observations, Spergel et al. (2003) obtained  $\Omega_b h^2 = 0.024 \pm 0.001$  and  $\Omega_m h^2 = 0.14 \pm 0.02$ . If we assume that baryons do not escape the dark matter overdensity they are associated with, the ratio of mass in baryons to

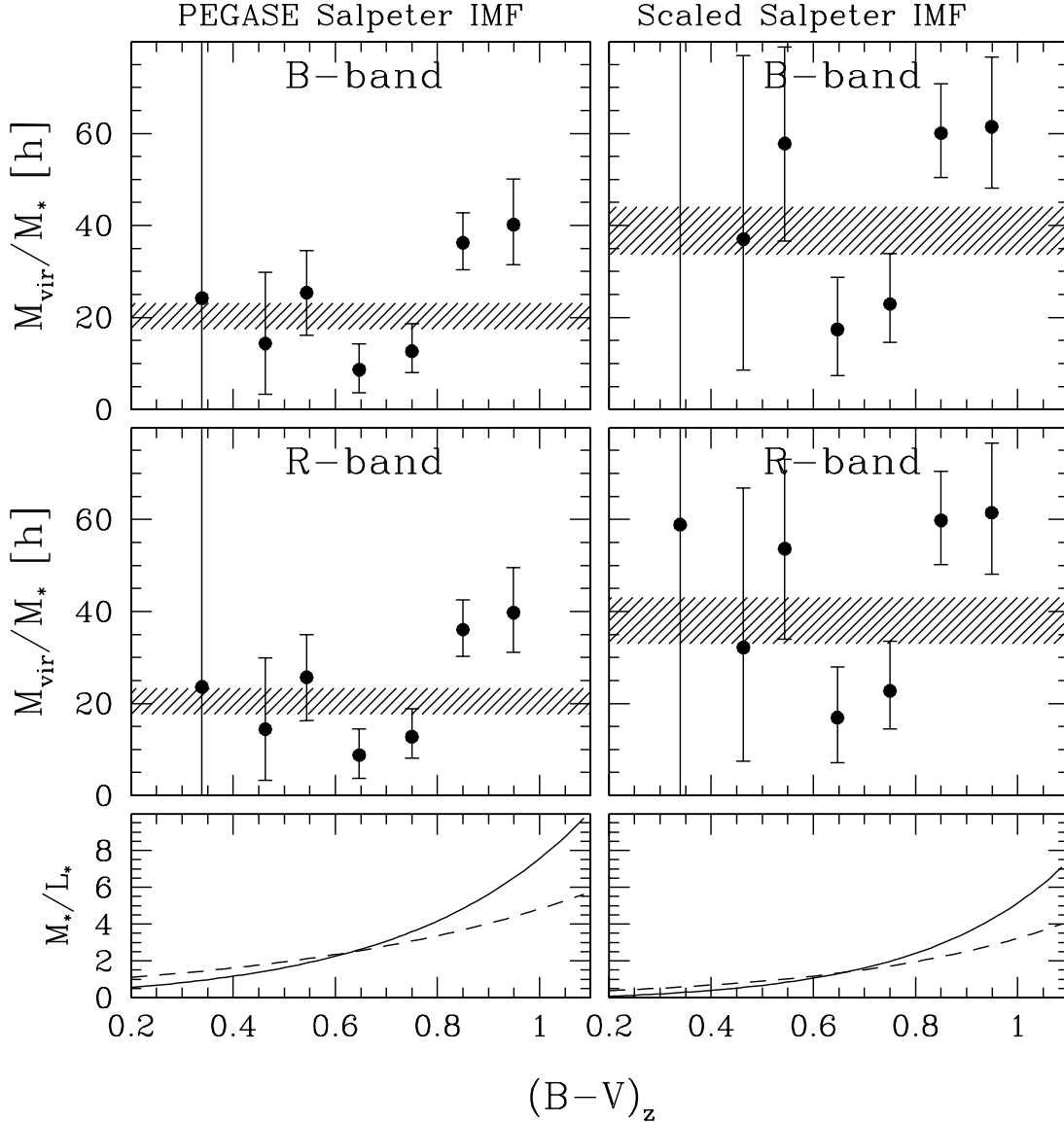


FIG. 10.—*Bottom*: Stellar mass-to-light ratios in the  $B$  band (solid lines) and  $R$  band (dashed lines) for the results from PEGASE models using a Salpeter IMF and metallicity  $Z = 0.02$  (left) and a scaled Salpeter IMF (right) from Table 1 of Bell & de Jong (2001). The mass-to-light ratios have been evolved to  $z = 0.32$ , which corresponds to the mean redshift of our lens sample. *Top*: Resulting ratios of virial mass and stellar mass for the  $B$ - and  $R$ -band data. For a given IMF, the results obtained in the different filters agree well, but it is clear that the mean values (shaded areas) depend strongly on the adopted IMF.

the total mass of the halo is  $M_{\text{bar}}/M_{\text{vir}} = \Omega_b/\Omega_m = 0.17 \pm 0.03$ . In the following, we also assume  $H_0 = 71 \text{ km s}^{-1} \text{ Mpc}^{-1}$ , which is the currently favored value.

For the PEGASE Salpeter model, this implies that the fraction of the mass in stars is  $0.070 \pm 0.011$  (average of the  $B$  and  $R$  value), whereas the scaled Salpeter IMF yields a lower value of  $0.037 \pm 0.005$ . Comparison with the value of  $\Omega_b/\Omega_m$  from CMB measurements suggests that only  $\sim 40\%$  and  $\sim 22\%$  of the baryons are converted into stars for the standard and scaled Salpeter IMFs, respectively. The actual results for the two filters considered here are indicated separately in Table 3 by  $f_{\text{bar} \rightarrow *}$ .

Table 3 also lists the average results when we consider blue and red galaxies separately. The implied star formation efficiencies for early-type galaxies are low. We note that similar efficiencies have been inferred for galaxy clusters (e.g., Lin et al. 2003).

Interestingly, our results imply that late-type galaxies convert a  $\sim 2$  times larger fraction of baryons into stars than early-type galaxies do. This result is robust, as it does not depend much

on the adopted IMF. Guzik & Seljak (2002) also found a factor of  $\sim 2$  difference in star formation efficiency between early and late-type galaxies, in good agreement with our findings. Hence, these results provide very important, direct observational constraints on the relative star formation efficiency during galaxy formation for different galaxy types.

These findings suggest that the mechanism for the formation of early-type galaxies is somehow more efficient in removing gas compared to late-type galaxies. Ram pressure stripping might be more prevalent, given that early-type galaxies are typically found in high-density regions, or they might form while developing strong winds that blow out most of the baryons.

Irrespective of the process responsible for ejecting baryons, the resulting galaxy will always have a stellar fraction that is greater or equal to the fraction of stars in its progenitors. If we consider the situation in which early-type galaxies form through mergers, it is clear that not all early-type galaxies can be the result of merging the late-type galaxies studied in this paper. Ejecting  $\sim 60\%$  of the stars during the merger process might seem to be an option,

TABLE 3  
STELLAR MASS AND BARYON FRACTIONS

SUBSET	PARAMETER	PEGASE		SCALED	
		<i>B</i>	<i>R</i>	<i>B</i>	<i>R</i>
All .....	$M_{\text{vir}}/M_*$	$14 \pm 2$	$15 \pm 2$	$27 \pm 4$	$28 \pm 4$
	$f_{\text{bar} \rightarrow *}$	$0.41^{+0.07}_{-0.05}$	$0.39^{+0.06}_{-0.05}$	$0.22^{+0.04}_{-0.03}$	$0.21 \pm 0.03$
	$f_{\text{bar}}^{\text{gal}}$	$0.070^{+0.012}_{-0.009}$	$0.065^{+0.010}_{-0.008}$	$0.037^{+0.005}_{-0.004}$	$0.035^{+0.005}_{-0.004}$
	$f_{\text{bar}}$				
$B - V < 0.8$ .....	$M_{\text{vir}}/M_*$	$9 \pm 2$	$10 \pm 3$	$17 \pm 5$	$18 \pm 5$
	$f_{\text{bar} \rightarrow *}$	$0.65^{+0.20}_{-0.14}$	$0.60^{+0.20}_{-0.12}$	$0.34^{+0.11}_{-0.08}$	$0.32^{+0.12}_{-0.07}$
	$f_{\text{bar}}^{\text{gal}}$	$0.11^{+0.03}_{-0.02}$	$0.10^{+0.03}_{-0.02}$	$0.057^{+0.018}_{-0.013}$	$0.055^{+0.021}_{-0.011}$
	$f_{\text{bar}}$				
$B - V > 0.8$ .....	$M_{\text{vir}}/M_*$	$26 \pm 4$	$28 \pm 4$	$42 \pm 6$	$45 \pm 6$
	$f_{\text{bar} \rightarrow *}$	$0.22 \pm 0.03$	$0.21 \pm 0.03$	$0.14 \pm 0.02$	$0.13 \pm 0.02$
	$f_{\text{bar}}^{\text{gal}}$	$0.038^{+0.006}_{-0.005}$	$0.036^{+0.005}_{-0.004}$	$0.024^{+0.004}_{-0.003}$	$0.022^{+0.004}_{-0.003}$
	$f_{\text{bar}}$				

NOTES.—Results for the PEGASE model using a standard Salpeter IMF and a scaled Salpeter IMF from Bell & de Jong (2001). These models have been evolved to a redshift of  $z = 0.32$  to allow for a direct comparison with the measurements. For different color selections, the rows list, respectively, the ratio of virial mass over stellar mass, the implied fraction of baryons transformed into stars, and the total visible baryon fraction in galaxies. Note that the results for the *B* and *R* bands are not independent. We have adopted a Hubble constant of  $H_0 = 71 \text{ km s}^{-1} \text{ Mpc}^{-1}$  and a universal baryon fraction of  $\Omega_b/\Omega_m = 0.17$  (e.g., Spergel et al. 2003).

but this is hard to envision without removing a similar fraction of the dark matter halo.

Hence, the progenitors of early-type galaxies must have had a low fraction of their mass in stars. This could be achieved if early-type galaxies (or their progenitors) formed early on without forming new stars at later times (because they lost their gas) and if later type galaxies sustained their star formation for a much longer time, thus building up a larger fraction of mass in stars. Recent estimates of the star formation rates of high-redshift galaxies suggest a qualitatively similar picture in which early-type galaxies formed the bulk of their stars very early on with a sharp drop in star formation rates at  $z \sim 2$  and less massive (late type) galaxies continue to form most of their stars at a later time and over a much longer period of time (e.g., McCarthy et al. 2004; Juneau et al. 2005).

### 5.3. Visible Baryon Fraction

In addition to stars, galaxies contain some gas, which needs to be included if we are to do a full accounting of the visible baryon contents of galaxies. Although the amount of molecular hydrogen is uncertain, the amount of neutral hydrogen is relatively well determined from 21 cm line studies. The relative amount of H I gas is a function of galaxy type, with late-type galaxies being more gas rich. We use the results from Roberts & Haynes (1994) for the  $M_{\text{H I}}/L_B$  ratio to estimate the amount of mass in gas (correcting the hydrogen mass to account for the primordial helium abundance). The inclusion of gas slightly raises the mass in detected baryons for the bluest galaxies, but this component is negligible for the red galaxies. Adding estimates for the amount of molecular hydrogen does not change the numbers either.

The resulting fraction of the mass in baryons in galaxies,  $f_{\text{bar}}^{\text{gal}}$ , is listed in Table 3 as well. Only for the blue galaxies, under the assumption of a standard Salpeter (1955) IMF, is the baryon fraction marginally consistent with the value determined from observations of the CMB (Spergel et al. 2003). However, as discussed earlier, the results for this model should be considered upper limits to the baryon fraction, given that the stellar mass-to-light ratios are too high to fit rotation curves (e.g., Bell & de Jong 2001). The results from the scaled IMF from Bell & de Jong are probably more representative of the actual baryon frac-

tions in galaxies, thus implying that a significant fraction of the gas must have been lost.

## 6. CONCLUSIONS

We have measured the weak-lensing signal as a function of rest-frame *B*-, *V*-, and *R*-band luminosity for a sample of “isolated” galaxies with photometric redshifts  $0.2 < z < 0.4$ . This selection of relatively isolated galaxies minimizes the contribution of group or cluster halos and nearby bright galaxies.

The photometric redshifts were derived by Hsieh et al. (2005) using  $BVR_C z'$  photometry from the Red-Sequence Cluster Survey. To add to the extensive study described in Hsieh et al. (2005), we subjected the photometric redshifts to tests that are unique to weak lensing. These results showed that the lensing signal around a sample of foreground galaxies scales with source redshift as expected. The photometric redshift distribution determined by Hsieh et al. (2005) suggests that the mean redshift of galaxies used in the measurement of the lensing signal by large-scale structure (Hoekstra et al. 2002c, 2002d) is somewhat higher than previously assumed. If correct, this would imply a somewhat lower value for the normalization of the matter power spectrum,  $\sigma_8$ , compared to the published results. The difference is expected to be less than  $\sim 10\%$ , but with the current data we cannot reliably quantify the size of the change.

Virial masses were determined by fitting an NFW model to the tangential shear profile. Note that intrinsic scatter in the mass-luminosity relation results in an underestimate of the mean virial mass for a galaxy of a given luminosity, as suggested by Tasitsiomi et al. (2004b). The magnitude of this effect depends on the assumed scatter, and we have ignored this in our analysis. We found that the virial mass as a function of luminosity is well described by a power law with a slope of  $\sim 1.5$ , with similar slopes for the three filters considered here. This result agrees with other observational studies (Guzik & Seljak 2002) and predictions from semianalytic models of galaxy formation (e.g., Kauffmann et al. 1999; Benson et al. 2000; van den Bosch et al. 2003). For a galaxy with a fiducial luminosity of  $10^{10} h^{-2} L_{B,\odot}$ , we obtained a mass  $M_{\text{vir}} = 9.9^{+1.5}_{-1.3} \times 10^{11} M_\odot$ . Converting this result to match the filter and definition for the mass used by Guzik & Seljak (2002) yields a mass of  $M_{200} = (11.7 \pm 1.7) \times 10^{11} h^{-1} M_\odot$  for a galaxy with a luminosity of  $1.1 \times 10^{10} h^{-2} h M_\odot/L_{g',\odot}$ , in

agreement with Guzik & Seljak (2002), who found  $M_{200} = (9.3 \pm 1.6) \times 10^{11} h^{-1} M_{\odot}$ .

We examined the efficiency with which baryons are converted into stars. To do so, we used the rest-frame  $B - V$  color as a measure of the mean stellar mass-to-light ratio. The color also provides a crude indicator of galaxy type (e.g., Robert & Haynes 1994). We considered a standard and a scaled Salpeter IMF (see Bell & de Jong 2001). The latter is more realistic, whereas the former yields stellar mass-to-light ratios that are too high to fit rotation curves of spiral galaxies.

Irrespective of the adopted IMF, we found that the stellar mass fraction is about a factor of 2 lower for early-type galaxies, as compared to late-type galaxies. Including the fraction of baryons in gas only increases the fraction of observed baryons slightly. Hence, our results suggest that galaxy formation is very inefficient in turning baryons into stars and in retaining baryons. These results provide important, direct observational constraints for models of galaxy formation.

Under the assumption that the scaled Salpeter IMF is correct, our results imply that late-type galaxies convert  $\sim 33\%$  of baryons into stars. Early-type galaxies do much worse, with an efficiency of  $\sim 14\%$ . This implies that the progenitors of early-type galaxies have a low fraction of their mass in stars. A possible explanation of this result is that early-type galaxies formed early on and stopped forming new stars because they lost most of their baryons (e.g., through winds or ram pressure stripping). If later type galaxies, on the other hand, continued to form stars, this would lead to a higher stellar mass fraction. Such a scenario is, at least qualitatively, in agreement with recent estimates of the star formation rates of high-redshift galaxies (e.g., McCarthy et al. 2004; Juneau et al. 2005).

We would like to thank the anonymous referee for a careful reading of the manuscript and providing useful suggestions that helped improve the paper.

#### REFERENCES

- Bartelmann, M. 1996, *A&A*, 313, 697  
 Bell, E. F., & de Jong, R. S. 2001, *ApJ*, 550, 212  
 Benson, A. J., Cole, S., Frenk, C. S., Baugh, C. M., & Lacey, C. G. 2000, *MNRAS*, 311, 793  
 Bernstein, G. M., & Norberg, P. 2002, *AJ*, 124, 733  
 Brainerd, T. G., Blandford, R. D., & Smail, I. 1996, *ApJ*, 466, 623  
 Bryan, G. L., & Norman, M. L. 1998, *ApJ*, 495, 80  
 Bullock, J. S., Kolatt, T. S., Sigad, Y., Somerville, R. S., Kravtsov, A. V., Klypin, A. A., Primack, J. R., & Dekel, A. 2001, *MNRAS*, 321, 559  
 Capak, P., et al. 2004, *AJ*, 127, 180  
 Connolly, A. J., Csabai, I., & Szalay, A. S. 1995, *AJ*, 110, 2655  
 Cowie, L. L., Barger, A. J., Hu, E. M., Capak, P., & Songaila, A. 2004, *AJ*, 127, 3137  
 Diemand, J., Moore, B., & Stadel, J. 2004, *MNRAS*, 353, 624  
 Dubinski, J., & Carlberg, R. G. 1991, *ApJ*, 378, 496  
 Faber, S. M., & Jackson, R. E. 1976, *ApJ*, 204, 668  
 Fioc, M., & Rocca-Volmerange, B. 1997, *A&A*, 326, 950  
 Fischer, P., et al. 2000, *AJ*, 120, 1198  
 Fukugita, M., Ichikawa, T., Gunn, J. E., Doi, M., Shimasaku, K., & Schneider, D. P. 1996, *AJ*, 111, 1748  
 Gladders, M. D., & Yee, H. K. C. 2000, *AJ*, 120, 2148  
 ———. 2005, *ApJS*, 157, 1  
 Guzik, J., & Seljak, U. 2002, *MNRAS*, 335, 311  
 Hayashi, E., et al. 2004, *MNRAS*, 355, 794  
 Hoekstra, H., Franx, M., & Kuijken, K. 2000, *ApJ*, 532, 88  
 Hoekstra, H., Franx, M., Kuijken, K., Carlberg, R. G., & Yee, H. K. C. 2003, *MNRAS*, 340, 609  
 Hoekstra, H., Franx, M., Kuijken, K., & van Dokkum, P. G. 2002a, *MNRAS*, 333, 911  
 Hoekstra, H., van Waerbeke, L., Gladders, M. D., Mellier, Y., & Yee, H. K. C. 2002b, *ApJ*, 577, 604  
 Hoekstra, H., Yee, H. K. C., & Gladders, M. D. 2002c, *ApJ*, 577, 595  
 ———. 2004, *ApJ*, 606, 67  
 Hoekstra, H., Yee, H. K. C., Gladders, M. D., Barrientos, L. F., Hall, P. B., & Infante, L. 2002d, *ApJ*, 572, 55  
 Hsieh, B. C., Yee, H. K. C., Lin, H., & Gladders, M. D. 2005, *ApJS*, 158, 161  
 Hudson, M. J., Gwyn, S. D. J., Dahle, H., & Kaiser, N. 1998, *ApJ*, 503, 531  
 Juneau, S., et al. 2005, *ApJ*, 619, L135  
 Kauffmann, G., Colberg, J. M., Diaferio, A., & White, S. D. M. 1999, *MNRAS*, 303, 188  
 Keeton, C. R., Kochanek, C. S., & Falco, E. E. 1998, *ApJ*, 509, 561  
 Lin, Y.-T., Mohr, J. J., & Stanford, S. A. 2003, *ApJ*, 591, 749  
 McCarthy, P. J., et al. 2004, *ApJ*, 614, L9  
 McKay, T. A., et al. 2001, *ApJ*, submitted (astro-ph/0108013)  
 Miralda-Escudé, J. 1991, *ApJ*, 370, 1  
 Moore, B., Quinn, T., Governato, F., Stadel, J., & Lake, G. 1999, *MNRAS*, 310, 1147  
 Navarro, J. F., Frenk, C. S., & White, S. D. M. 1995, *MNRAS*, 275, 56  
 ———. 1996, *ApJ*, 462, 563  
 ———. 1997, *ApJ*, 490, 493  
 Parker, L. C., Hudson, M. J., Carlberg, R. G., & Hoekstra, H. 2005, *ApJ*, in press  
 Roberts, M. S., & Haynes, M. P. 1994, *ARA&A*, 32, 115  
 Salpeter, E. E. 1955, *ApJ*, 121, 161  
 Seljak, U. 2002, *MNRAS*, 334, 797  
 Sheldon, E. S., et al. 2004, *AJ*, 127, 2544  
 Smith, D. R., Bernstein, G. M., Fischer, P., & Jarvis, M. 2001, *ApJ*, 551, 643  
 Spergel, D. N., et al. 2003, *ApJS*, 148, 175  
 Tasitsiomi, A., Kravtsov, A. V., Gottlöber, S., & Klypin, A. A. 2004a, *ApJ*, 607, 125  
 Tasitsiomi, A., Kravtsov, A. V., Wechsler, R. H., & Primack, J. R. 2004b, *ApJ*, 614, 533  
 Tully, R. B., & Fisher, J. R. 1977, *A&A*, 54, 661  
 van Albada, T. S., & Sancisi, R. 1986, *Philos. Trans. R. Soc. London A*, 320, 447  
 van den Bosch, F., Yang, X., & Mo, H. J. 2003, *MNRAS*, 340, 771  
 van Dokkum, P. G., & Franx, M. 1996, *MNRAS*, 281, 985  
 Verheijen, M. A. W. 2001, *ApJ*, 563, 694  
 Wilson, G., Kaiser, N., Luppino, G. A., & Cowie, L. L. 2001, *ApJ*, 555, 572  
 Wirth, G. D., et al. 2004, *AJ*, 127, 3121  
 Wright, C. O., & Brainerd, T. G. 2000, *ApJ*, 534, 34  
 Yee, H. K. C., et al. 2000, *ApJS*, 129, 475